33RD CONGRESS
OF THE INTERNATIONAL COUNCIL
OF THE AERONAUTICAL SCIENCES
STOCKHOLM, SWEDEN, 4-9 SEPTEMBER, 2022

ICAS 2022 SWEDEN

MULTIPOINT AERODYNAMIC DESIGN OF A NACELLE FOR AN ELECTRIC FAN

Vinícius Tavares Silva[1], Aravindhan Venkatesh[1], Marcus Lejon[2], Anders Lundbladh[2], Carlos Xisto[1]

[1]Chalmers University of Technology
[2]GKN Aerospace Sweden AB

Abstract

Attention to aircraft electrification has been growing quickly since such technology carries the potential of drastically reducing the environmental impact of aviation. This paper describes the re-design of a nacelle for an electric fan, which is developed as part of the EleFanT (Electric Fan Thruster) project. A multipoint nacelle design approach was carried out. Initially the nacelle shapes were optimized for a cruise condition by employing an evolutionary genetic algorithm (GA). The flow field around the nacelles was calculated by conducting 2D axisymmetric computational fluid dynamics (CFD) simulations, and the objective functions were computed by means of thrust and drag bookkeeping. It was found that the optimizer favored two types of nacelle shapes that differed substantially in geometry. The designs were referred to as low spillage and high spillage types. The optimum low spillage and high spillage cases were selected and investigated further by the means of 3D CFD simulations at cruise and at an end of runway takeoff condition, where the nacelle is subjected to high angle of attack. Whilst the low spillage case provided a slightly better performance at cruise, it presented high levels of distortion and boundary layer separation at takeoff, requiring a substantial shape modification. The high spillage case performed well at takeoff; however, supersonic velocities could be observed at the cowling when it was subjected to incoming flow at an angle of attack. Nonetheless, such problem was easily corrected by drooping the inlet. Due to its superior performance at takeoff, the drooped high spillage design type was recommended.

Keywords: Nacelle; Electric aircraft; Electric propulsion; Computational fluid dynamics; Optimization

1. Introduction

The European aviation industry has set a target for net zero CO_2 emissions from all flights within and departing from the European Union to be achieved by 2050 and established an ambitious decarbonization roadmap [1]. To attain such a challenging goal, the current aeroengines will need to undergo significant technology improvements. CFM's RISE (Revolutionary Innovation for Sustainable Engines) program is developing hybrid electric propulsion technologies, by combining gas turbines and electrical motors, as a possible solution for the decarbonization of air transport [2]. Another technological breakthrough would be to make use of an electric motor to drive a propeller or fan, powered by fuel cells or batteries. GKN Aerospace, in collaboration with KTH Royal Institute of Technology, is developing fan technology for regional electric aircraft as part of the EleFanT (Electric Fan Thruster) project. The work is supported by the Swedish Energy Agency and will study performance, aerodynamic design, noise, structural aspects and manufacturing technology for an electric ducted fan. One of the aspects of the development of such a propulsion system is to design an efficient and robust nacelle and consider the effects of its coupling with the fan. The design of such a nacelle, taking into account asymmetric flow field and different operating conditions, is covered by the present study.

The feasibility of electric and hybrid aircraft technologies has recently become a strong subject of research and discussion. Bari et al. [3] analyzed several powertrain technologies that could allow electric powered aircraft to perform intra-continental flights, concluding that the most promising future technology is hydrogen fuel cells. Wroblewski et al. [4] conducted a feasibility study of a hybrid electric commercial transport aircraft, concluding that, with future improvement in battery specific energy density, it could be possible to carry out a mission with similar range to that of the mean of all global flights. On the propulsion level, Huang et al. [5] conducted a propeller design for a hypothetical electric aircraft aiming at low noise, reaching the conclusion that the installation of multiple propellers could potentially reduce the total aircraft noise.

Extensive research has been conducted on the design of advanced nacelles for high bypass turbofan engines. Christie et al. [6, 7] have developed novel Class Shape Transformation (CST)-based methods for designing nacelles and inlets. Tejero et al. [8, 9] have developed a CST-based framework for aero-engine nacelles multi objective optimization. Furthermore, CST curves were also widely used for exhaust nozzles design and optimization [10–12]. Silva et al. [13] and Peters at al. [14] have developed methodologies for multipoint design of ultra-high-bypass turbofan nacelles with ultrashort inlets. Nonetheless, nothing has been found in literature that aimed specifically at the design of nacelles for aircraft powered by electric fans. This paper describes the initial design efforts to achieve an efficient and robust a nacelle for the thruster considered in the EleFanT project. A preliminary 2D optimization is presented for the aircraft in cruise, followed by a study of how the 3D effects and off-design operating conditions can impact on the design of nacelles for electric fans.

2. Methodology

The design of a nacelle requires several compromises since conflicting requirements must be satisfied for different operating conditions. The nacelle is shaped so that it provides minimum drag at cruise. A further goal is to prevent boundary layer separation inside the inlet and to provide low levels of total pressure distortion, so that the fan can operate stably for a wide range of operating conditions. This is especially critical at low speed and high-incidence conditions, encountered at the end of runway during take-off, initial climb and crosswind. Such conflicting requirements often demand an asymmetric shaping of the nacelle. Usually, the lower part needs to be thicker and blunter so that the boundary layer can be maintained attached, or with moderate levels of separation, during the entire flight envelope.

An integrated aerodynamic design framework has been built to perform the design of nacelles for electric fans. The framework is comprised of parametric geometry generation, automatic mesh generation, flow field solution via computational fluid dynamics (CFD), and performance assessment by means of thrust and drag bookkeeping. The tool is capable of designing both 2D axisymmetric and 3D asymmetric nacelles, taking into account the most critical operating conditions within the flight envelope. Moreover, the design was combined with an evolutionary genetic algorithm in order to perform a preliminary 2D axisymmetric optimization at cruise. The following sections describe in detail each one of the elements of the developed framework.

2.1 Parametric geometry generation

The Class Shape Transformation (CST) method [15, 16] was used to describe the nacelles' geometry. It has shown to be a robust and versatile approach for parametric geometry representation, allowing for the construction of smooth shapes with a small number of design variables. The CST method is based on products between class functions $C(\psi)$ and shape functions $S(\psi)$. The class function determines the basic profile, which is transformed by the shape function, usually defined by a Bernstein polynomial.

A full 2D nacelle geometry is defined by joining five different CST curves, representing the inlet, fan-cowl, nozzle, core-cowl, and spinner. The major geometric parameters for the nacelle and nozzle geometric representation are shown in Figure 1a and Figure 1b, respectively. The spinner shape has a conical tip and a cambered rear cone, sometimes referred to as coniptical. This shape combines the high aerodynamic performance of an elliptical spinner and low tendency for ice accretion of a conical spinner [17, 18].

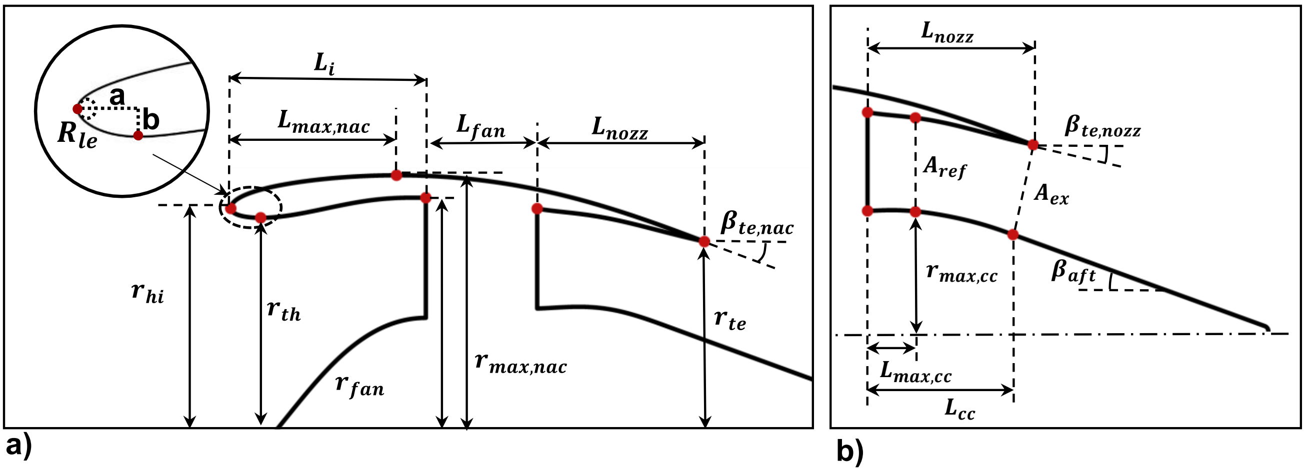

Figure 1 – Major geometric parameters of a 2D nacelle for an electric fan.

Table 1 depicts the main design variables for the nacelle external part and for the inlet duct. The fan radius r_{fan} and length L_{fan} were kept constant since the nacelle is being optimized for an existing fan design. Furthermore, the length of the nacelle L_I was maintained unchanged, since a very short inlet is desirable for low drag and weight. However, the inlet must be able to provide a smooth flow, free of boundary layer separation, under off-design conditions. The inlet length was selected so that $L_I/D_{fan} = 0.42$, which characterizes a short and advanced inlet, but not an extreme design, resting assured that the nacelle could be shaped to fulfill the most stringent off-design criteria.

Table 1 – Nacelle optimization variables

Description	Parameter
Contraction ratio	$r_{\mathrm{hi}}^2/r_{\mathrm{th}}^2$
Lip aspect ratio	a/b
Highlight radius to maximum radius ratio	r_{hi}/r_{max}
Maximum radius to fan radius ratio	r_{max}/r_{fan}
Axial position of maximum diameter	$f_{max,nac} = L_{max,nac}/L_{nac}$
Cowl non-dimensional leading-edge radius of curvature	$f_{le,nac} = \dfrac{R_{le,nac} f_{max,nac} L_{nac}}{\left(r_{max,nac} - r_{\mathrm{hi}}\right)^2}$
Inlet non-dimensional leading-edge radius of curvature	$f_{le,i} = \dfrac{R_{le,i} f_{th} L_I}{(r_{th} - r_{\mathrm{hi}})^2}$
Nacelle boattail angle	$\beta_{te,nac}$

* f_{th} is the axial position of the inlet throat (a/L_I)

The main design variables for the nozzle, used for the optimization studies presented later in this work, are shown in table 2.

Table 2– Nozzle optimization variables

Description	Parameter
Nozzle area ratio	A_{ref}/A_{ex}
Maximum core cowl radius to fan radius ratio	$r_{max,cc}/r_{fan}$
Axial position of maximum diameter	$f_{max,cc} = L_{max,cs}/L_{cc}$
Nozzle trailing edge angle	$\beta_{te,nozz}$
Aft body cone angle	β_{aft}

For the inlet, fan cowling and nozzle 3D design, two dimensional parametrizations are performed for the positions of $\phi = 0^o$, $\phi = 90^o$ and $\phi = 180^o$, referred to as crown, maximum half-breadth (MHB) and keel, where ϕ is the azimuth angle in a cylindrical coordinate system. To obtain a 3D nacelle shape, sinusoidal interpolations of the r (radial coordinate) and x (axial coordinate) are performed circumferentially between the crown, MHB and keel. The left nacelle half ($180^o \leq \phi \leq 360^o$) is a mirror image of the first one. The core cowl and spinner are axisymmetric. Figure 2 depicts an example of a 3D nacelle shape. The parametrization positions were chosen to allow geometric control where local flow effects are critical. The crown should be shaped for minimum drag, whereas the keel geometry plays a fundamental role in preventing separation at high incidence and low-speed operational conditions. Moreover, the side parametrization is important to prevent separation and minimize flow distortion into the fan under crosswind conditions. Normally, nacelles for aeroengines installed under-the-wing, are drooped so that the inlet is better aligned with the incoming flow and drag is reduced at cruise. Therefore, an additional design variable is added for the 3D geometries, which is the droop angle θ_d.

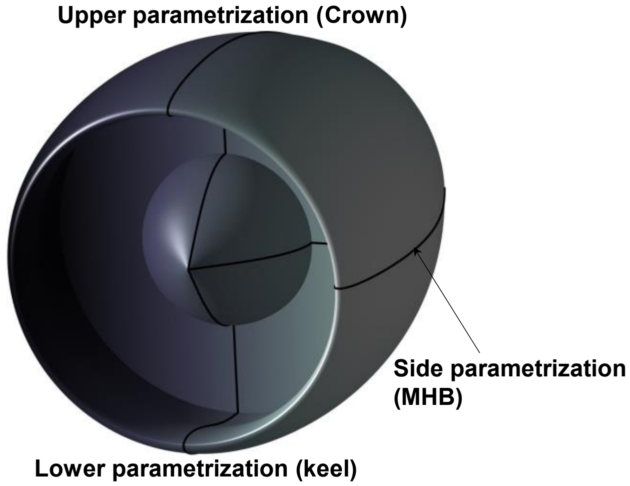

Figure 2 – Nacelle 3D geometry definition.

2.2 Numerical approach

Two-dimensional and three dimensional multiblock structured meshes are automatically generated using the ANSYS ICEM CFD meshing software. The computational domain is defined between the nacelle and a cylindrical far-field with length and diameter equal to 60 times the fan diameter. In order to resolve the viscous sub-layer, the first cell height was set so that $y^+ < 1$.

The flow field around the nacelle was computed by the means of 2D axisymmetric and 3D computational fluid dynamics (CFD). The commercial software ANSYS FLUENT was used to solve the Reynolds-Averaged Navier-Stokes (RANS) equations. The pressure-based solver and the pressure-velocity coupled algorithm were selected. The chosen turbulence closure model was the Menter's k-ω shear stress transport (SST) model. The least squares cell-based method was used for computation of the flow field gradients and a second order upwind scheme was employed to interpolate the convection terms along with the specific dissipation rate and the turbulence kinetic energy.

2.2.1 Boundary conditions

The schematic representation of the CFD domain and boundary conditions (BC) for the 2D axisymmetric and 3D simulations is shown in Figure 3a and Figure 3b, respectively. For the 2D axisymmetric calculations a pressure outlet BC is set at the fan face, where a constant static pressure is specified, and the mass flow is targeted to match the mass flow computed at the fan exit. At the fan exit, a pressure inlet BC was chosen, where total pressure and total temperature are set. The domains upstream and downstream of the nacelle are defined as pressure inlet and pressure outlet, respectively, whereas the upper domain was defined as a slip wall. For the 3D simulations, a pressure outlet BC is set at the fan face, where a static pressure profile is set, calculated by means of the Modified Parallel Compressor (MPC) method [13], which is briefly described in section 2.2.2. At the fan exit a mass flow inlet BC is used, where the mass flow and total temperature are specified. The mass flow computed at the fan face is targeted there, to assure conservation of mass throughout the engine. The external domain is defined as a pressure far-field BC, where the static temperature, static pressure, Mach number and flow direction are specified.

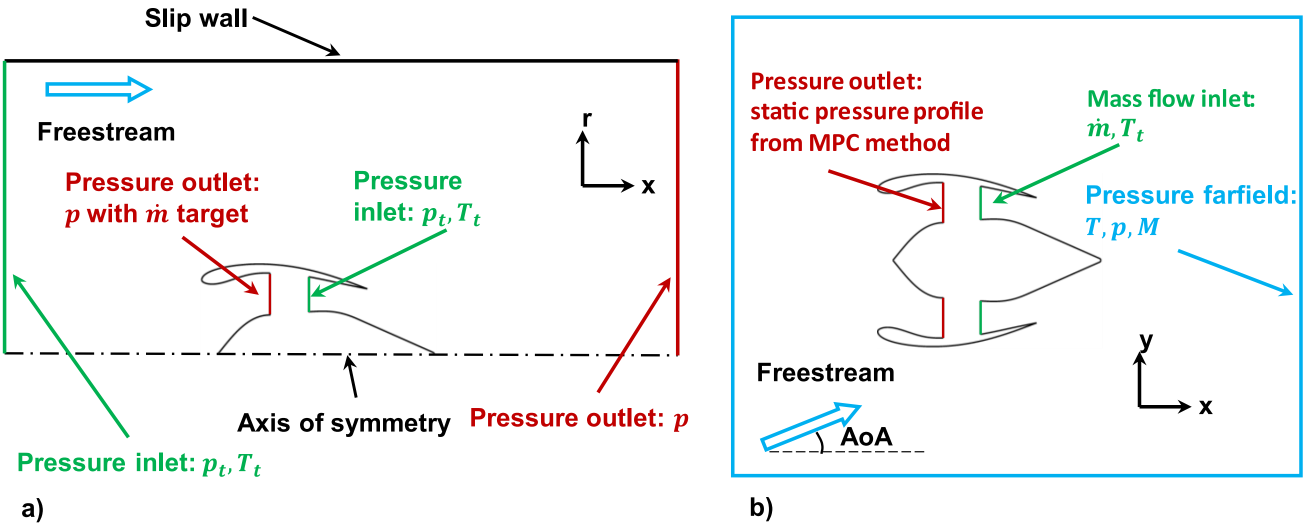

Figure 3 – Boundary conditions and CFD domain schematic representation for: a) 2D axisymmetric and b) 3D simulations.

2.2.2 Fan-inlet coupling

The coupling between the inlet and the fan was approached by using the modified parallel compressor (MPC) method, which was developed and validated by Silva et al. [13]. The method estimates the static pressure profile at the fan face, by using the field variables, a fan speed line, and the assumption that the fan discharges at constant static pressure. The MPC method is based on the classical parallel compressor theory, which consists of splitting the compressor or fan into two sectors, both discharging at the same static pressure but with distinct inlet total pressures. The sector with lowest inlet total pressure will operate with a highest-pressure ratio and vice-versa. The higher the total pressure distortion levels, the harder the fan needs to work, and the lower will be the inlet static pressure. This fundamental concept was adapted to CFD applications in the MPC method, which was shown to work well particularly for distorted cases, where the total pressure drops significantly at a certain portion of the fan face [13]. Moreover, it is a robust method, which requires a low computational cost and only few input data. It is also considered very useful for preliminary nacelle designs, when the geometry of the fan blades is not yet available.

2.3 Performance Metrics

This section describes the parameters necessary to quantify the nacelle, inlet and nozzle performance.

2.3.1 Thrust and drag bookkeeping

A modified near-field bookkeeping method, which involves integration both over the nacelle surfaces and along the captured streamtube, was used to calculate thrust, drag and assess the nacelle aerodynamic performance. For a freestream aligned with the domain's x-axis, the conservation of axial momentum can be applied to the captured and post-exit streamtubes leading to the following equation for the standard net thrust [19, 20]:

$$T_N = \int_{S_0} \left[\rho u(\vec{V}\cdot\vec{n}) + (p-p_\infty)n_x - (\vec{\tau}_x\cdot\vec{n})\right]dS - \int_{S_{\text{out}}} \left[\rho u(\vec{V}\cdot\vec{n}) + (p-p_\infty)n_x - (\vec{\tau}_x\cdot\vec{n})\right]dS \tag{1}$$

where S_0 is the captured streamtube area, far upstream of the engine, and S_{out} includes all the surfaces wetted by the exhaust jet. The pre-entry force ϕ_{pre} is defined as:

$$\phi_{\text{pre}} = \int_{S_0 \cup S_{\text{in}}} \left[\rho u(\vec{V}\cdot\vec{n}) + (p-p_\infty)n_x - (\vec{\tau}_x\cdot\vec{n})\right]dS \tag{2}$$

where S_{in} is comprised of all the inlet surfaces wetted by captured streamtube. The integrated force on the fan-cowl ϕ_{FC} can be defined as:

$$\phi_{FC} = \int_{S_{FC}} [(p-p_\infty)n_x - (\vec{\tau}_x\cdot\vec{n})]dS = \left(\phi_p + \phi_f\right)_{S_{FC}} \tag{3}$$

where ϕ_p is the skin pressure force, ϕ_f the skin friction force. The net propulsive force F_N, which is defined as the thrust minus drag, can be written as follows:

$$F_N = T_N - \left(\phi_p + \phi_f\right)_{S_{FC}} - \phi_{pre} \tag{4}$$

The configuration drag can be expressed as follows:

$$D_c = \left(\phi_p + \phi_f\right)_{S_{FC}} + \phi_{pre} \tag{5}$$

The drag coefficient c_d can be defined by using the fan face area A_{fan} as reference:

$$c_d = \frac{D_c}{q_\infty A_{fan}} \tag{6}$$

Where q_∞ is the dynamic pressure, defined as $0.5\rho_\infty V_\infty^2$.

2.3.2 Inlet aerodynamic performance

For the inlet duct, the aerodynamic performance can be assessed by the means of the mass flow ratio MFR, intake pressure recovery η_i and the distortion coefficient DC_{60}. The MFR, consists of an aerodynamic reference parameter for the inlet and it is defined as the ratio of the stream-tube captured area, A_∞, and the highlight area, A_{hi}, as follows:

$$MFR = \frac{A_\infty}{A_{hi}} \tag{7}$$

The intake pressure recovery is a measure of how much of the free-stream total pressure is retained after the flow passed through the inlet. It can be defined as follows:

$$\eta_i = \frac{p_{\mathrm{t},\infty}}{p_{t1}} \tag{8}$$

The DC_{60} coefficient is a parameter commonly used to assess the total pressure distortion level, which is defined as:

$$DC_{60} = \frac{\overline{p}_{t2} - \overline{p}_{t2,60}}{\overline{q}} \tag{9}$$

where $\overline{p}_{t2}$ and $\overline{q}$ are the area averaged total and dynamic pressures at the fan face, and $\overline{p}_{t2,60}$ is the area averaged total pressure for a 60-degree sector, normally defined at the most distorted portion in the fan face.

2.3.3 Nozzle aerodynamic performance

The aerodynamic performance of a nozzle can be expressed in terms of the thrust and discharge coefficients, referred to as C_T and C_D respectively. The former accounts for thrust losses dues to non-isentropic phenomena such as formation of shear layers between the freestream and the nozzle stream, shear stresses on the walls, and shock waves in choked nozzles. The latter is a measure of effective area reduction due to total pressure losses and blockage caused by boundary layer growth. The definitions of C_D and C_T used in this paper are in accordance with the formulation described in [21]. The discharge coefficient can be defined as the ratio between the actual mass flow to the ideal isentropic mass flow passing through the nozzle exhaust area A_{ex}, where the ideal mass flow $\dot{m}_i$ is calculated from the isentropic relations for an ideal gas, as follows

$$\dot{m}_{\mathrm{i}} = A_{ex} p_t \left(\frac{1}{\lambda}\right)^{\frac{1}{\gamma}} \sqrt{\frac{2\gamma}{(\gamma-1)RT_t}\left(1-\left(\frac{1}{\lambda}\right)^{\frac{\gamma-1}{\gamma}}\right)} \tag{10}$$

where the nozzle pressure ratio, λ, is defined as

$$\lambda = \begin{cases} p_t/p_\infty\,, if\;\; p_t/p_\infty < PR_{crit} \\ PR_{crit}, if\;\; p_t/p_\infty > PR_{crit} \end{cases} \tag{11}$$

and the critical pressure ratio, PR_{crit}, as

$$PR_{crit} = \left(\frac{\gamma+1}{2}\right)^{\frac{\gamma}{\gamma-1}} \tag{12}$$

The nozzle discharge coefficient can thus be written as

$$C_D = \frac{\dot{m}}{\dot{m}_i} \tag{13}$$

The thrust coefficient is defined as the ratio of the actual gross thrust T_{gross} to the ideal thrust produced by the nozzle. The latter is defined as the product of the actual mass flow and the ideal velocity V_i, resulting from an isentropic expansion to the ambient pressure. V_i and C_T can be respectively written as follows

$$V_\mathrm{i} = \sqrt{\frac{2\gamma R T_t}{(\gamma-1)}\left(1-\left(\frac{1}{p_t/p_\infty}\right)^{\frac{\gamma-1}{\gamma}}\right)} \tag{14}$$

$$C_T = \frac{T_{gross}}{\dot{m}V_i} \tag{15}$$

The nozzle gross thrust can be expressed as

$$T_{gross} = V_{ex} + (p_{ex} - p_\infty)A_{ex} \tag{16}$$

Where p_{ex} and V_{ex} are the average pressure and velocity at the nozzle exhaust plane, respectively.

2.4 Optimization procedure – 2D axisymmetric computations

The optimization procedure was comprised of two distinct parts, where the nozzle and nacelle were optimized separately. The initial step was to conduct a preliminary nozzle optimization, to obtain a baseline geometry to be used in the inlet and nacelle optimization studies. The consecutive step utilizes the obtained best optimum nozzle design and optimized solely the inlet and fan cowling shapes. The final optimum is then used for the 3D design, which takes into account the cruise and takeoff conditions. The design variables used for the nacelle and nozzle optimization are shown in Table 1 and Table 2, respectively.

The optimization process starts by performing an initial sampling of the design space, the Latin Hypercube Sampling (LHS) method was used for fulfilling this step. The 2D nacelle and nozzle geometries are generated by using the CST method for parametric definition of aerodynamic shapes and consecutively meshed by using the ANSYS ICEM meshing software. The flow field around the nacelle and nozzle is calculated by means of 2D axisymmetric CFD, using the solver ANSYS FLUENT and the objective functions can be calculated by using the performance metrics described in section 2.3. An evolutionary genetic algorithm (GA) receives the data from the CFD simulations and searches within the design space for the optimum geometries. A MATLAB code was built to link all the elements of the framework and fully automatize the design procedure.

For the nozzle optimization, a non-dominated Sorting Genetic Algorithm (NSGA-II) algorithm was employed. The chosen objective functions were the discharge and thrust coefficients C_D and C_T, since together they account for both losses in thrust and flow blockage. When optimizing a nozzle geometry, care must be taken so that the operating point is kept fixed throughout the entire design space, i.e., the optimizer should not be allowed to search for off-design conditions. To fulfill this requirement, the nozzle exit area is explicitly modified to provide the design point mass flow. For each optimizer's evaluation, an internal loop was created to iterate on the exit area. The maximum number of iterations necessary for achieving convergence was 4. Nonetheless, it is worth mentioning that, by fixing the stagnation pressure at the fan exit, the fan pressure ratio might slightly change for different geometries, depending on the total pressure loss at the inlet. This effect was negligible for the nozzle optimization because the inlet and cowling geometries were kept unchanged.

For the nacelle and inlet optimization, a surrogate model, using a Gaussian Processes Regression (Kriging interpolation), is first built by using the initial design set and is constantly updated within the optimization the loop, using the inputs from the CFD calculations. A simple GA is used to find the optimum designs. The GA is guided by the surrogate model to the regions of the design space where the optimum is likely to be located, thus reducing the necessary amount of CFD simulations. The major goal when designing a nacelle is to achieve minimum drag for the cruise condition, therefore, the configuration drag c_d was chosen as the objective function. Although other performance metrics should be evaluated for different segments of the flight envelope, a single objective optimization is deemed to be a fast and useful preliminary study for providing a baseline design and performing the initial space exploration.

Besides providing a low external drag, the inlet needs to assure a low level of flow distortion at the fan face, and low total pressure loss through the inlet. The intake pressure recovery η_i is a straightforward measure of loss in stagnation pressure. Therefore, a constraint was added so that all the designs with $\eta_i < 0.999$ were considered to be unfeasible. Moreover, constraints were added to the nacelle local thickness, so that the obtained optimum would be manufacturable. The optimization process was carried out for 60 individuals over a total of 60 generations. The maximum number of calls for the original model was limited to 2000.

2.5 Overall design procedure

The design procedure starts by performing the aforementioned 2D axisymmetric optimization for the cruise (design point) condition. The optimum design is then utilized as a baseline for the 3D studies. Two operating conditions were chosen for the 3D cases as follows: mid cruise with angle of attack (AoA) and takeoff with high AoA, at end of the runway. The initially optimized 2D axisymmetric design is locally reshaped in order to attain a non-axisymmetric shape capable of operating well under the selected operating conditions. For the cruise condition, the goal is to obtain a low drag, whilst for high AoA, the intent is to avoid separation inside the inlet, or, at least, achieve low levels of distortion.

A small regional aircraft is considered to provide relevant flight conditions for the thruster. At the cruise condition, the altitude is set as 25000 ft and the Mach number M_∞ is set as 0.5. The AoA was chosen to be 4^o, which was selected considering the aircraft AoA added to a local incidence angle, caused by upwash from the wings. For the takeoff end of runway condition, the aircraft is at sea level with $M_\infty = 0.18$ and $AoA = 22^o$. The takeoff AoA was defined based on a realistic AoA at which the aircraft reaches the maximum takeoff lift coefficient, $C_{l,max}$, with addition of a local incidence effect to account for the wing upwash. It is worth nothing that this is a critical condition to be taken into account solely for the design purpose, and it is not supposed to happen throughout the aircraft mission.

3. Results

The major results obtained in the present study are reported in this section, which is divided into 3 main parts: 1) Mesh independency study, 2) 2D axisymmetric studies, 3) 3D studies.

3.1 Mesh independency study

A mesh independency study was carried out for the 2D and 3D cases, to guarantee that the utilized grid was fine enough to compute the nacelle drag. To assure a consistent mesh refinement, a global scaling factor was applied to the 2D and 3D domains, increasing the number of nodes in all directions. The height of the wall adjacent cells was kept constant across the domains, so that the wall y^+ would be below unity. For the 2D axisymmetric case, five grid levels were tested. The number of cells N varied from approximately 11.79×10^3 for the coarsest mesh to 335.49×10^3 for the finest. The results are shown in figure 4a. Four grid sizes were studied for the 3D CFD simulations. N varied from approximately 3.95×10^6 for the coarsest mesh to 14.50×10^6 for the finest. The results are shown in figure 4b.

The grid with 65.145×10^3 elements was selected for conducting the 2D axisymmetric simulations presented later in this paper, because it presented a difference of -0.09%, compared with the finest grid. For the 3D CFD simulations, the mesh with 9.75×10^6 elements was chosen, since its c_d differed from the finest grid's by 0.02%.

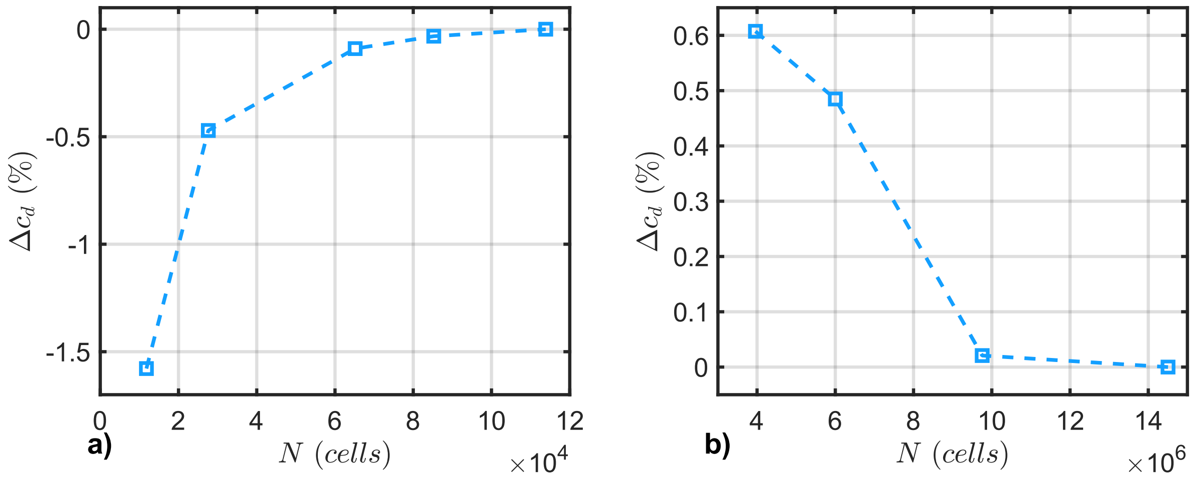

Figure 4 – Mesh independency study for a) 2D axisymmetric CFD simulations and b) 3D CFD simulations. Δc_d is the percentage difference between the c_d of a given mesh and that of the finest mesh.

3.2 Two-dimensional axisymmetric studies

This subsection presents the main results of the 2D optimization studies and is divided into two parts: 1) nozzle optimization and 2) nacelle and inlet optimization

3.2.1 Nozzle optimization

As mentioned in section 2.4, the objective functions for this study were C_D and C_T, the design variables and respective ranges are depicted in table 1. The study was carried out through 20 generations with 20 individuals each. The population and Pareto front obtained from the nozzle optimization are depicted in Figure 5. Ultimately, the nozzle should be able to provide a high thrust, and, consequently, a high C_T, therefore, priority was given to C_T over C_D in the choice of a single design among the pareto front. The highest C_T was thus selected for the successive nacelle and inlet optimization studies.

A combined search for C_T and C_D is, however, advantageous because it does not allow the optimizer to search for designs with excessive flow blockage, that could force the engine to operate in off-design conditions. Particularly for this work, where the exit area is being iterated to keep the engine operating point fixed, a very low C_D would mean that a high increase in area would be necessary to achieve the desired mass flow. For the selected design, highlighted in red in Figure 5, the nozzle coefficients are: $C_D = 0.9298$ and $C_T = 0.9776$.

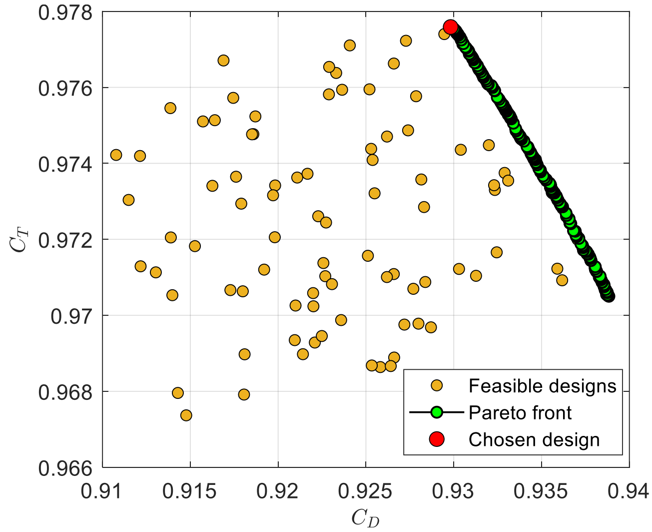

Figure 5 – Population and pareto front plot for the nozzle optimization.

3.2.2 Nacelle and inlet optimization

For the nacelle and inlet optimization, the optimum nozzle geometry was used and kept unchanged, as well as its exit area. Although this does not necessarily assure that the engine will be operating at the same point throughout the entire design space, it was assumed that, for a fixed nozzle geometry and exit area, the impact of the external flow field on the engine's mass flow and pressure ratio would be low for the good designs. This way the iteration on the exit area could be avoided and the optimization process accelerated.

Figure 6 shows the correlation between the objective function and other relevant performance metrics, where c_d^* is the drag coefficient normalized by the c_d obtained for the low spillage design. It could be observed that the optimizer was searching for two major design types that, despite of being considerably distinct geometrically, were providing similar levels of c_d. Such designs are highlighted in figure 6 and were referred to as low spillage and high spillage and will be discussed next.

The low spillage nacelle is characterized by a highly cambered shape, and a low highlight area. To decrease the drag caused by spillage, and consequently ϕ_{pre}, r_{hi} is moved downwards, and r_{hi}/r_{max} decreases. For very low r_{hi}/r_{max}, η_i falls below 0.999, and the design is considered unfeasible. As the highlight area is low, such type of design has a high MFR. The high spillage nacelle comprises a high highlight area and thus a high r_{hi}/r_{max} value and an unexpectedly low MFR, leading to a large ϕ_{pre}, however, better values of η_i.

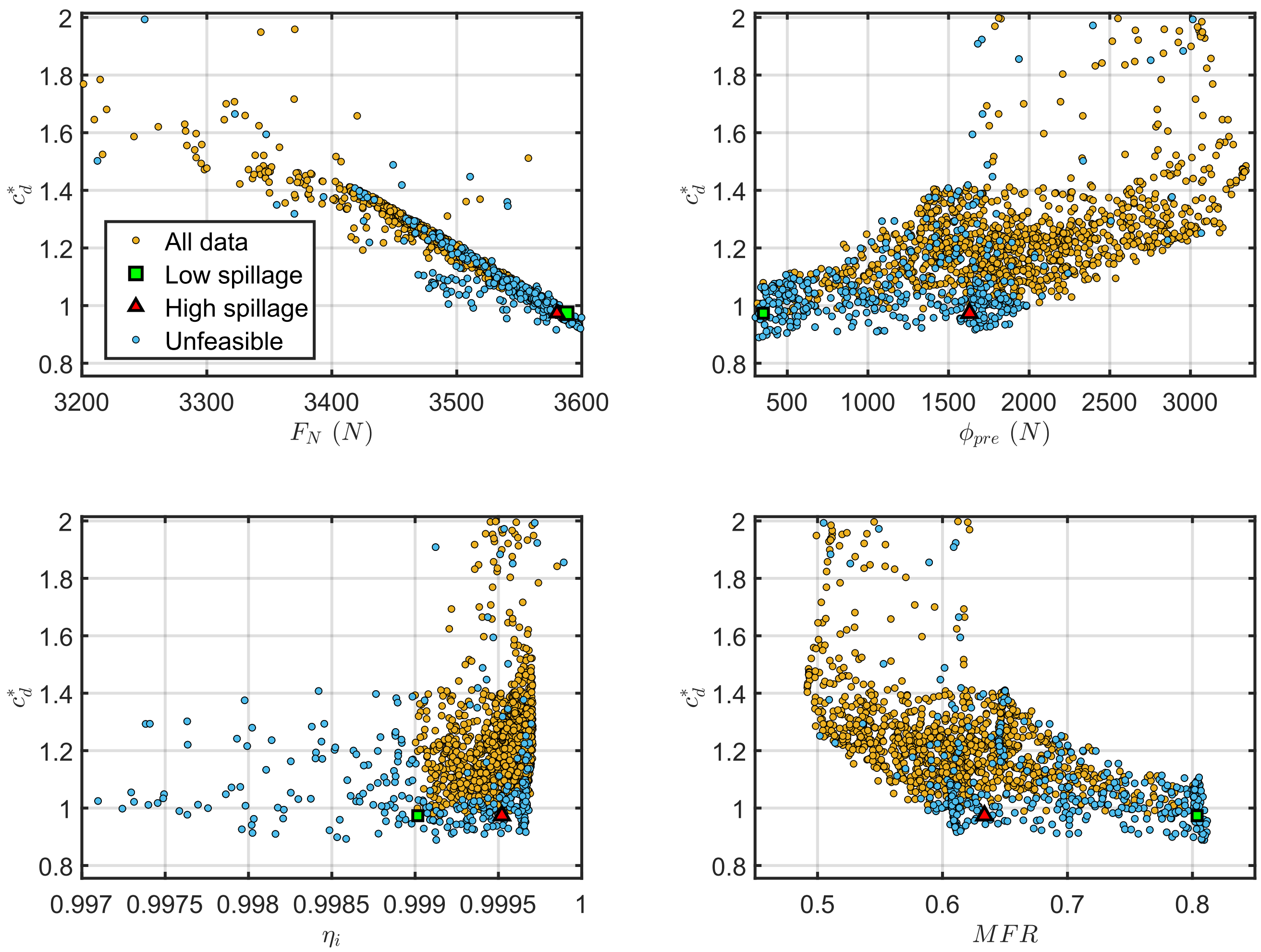

Figure 6 - Correlation between the objective function and other performance metrics. The designs marked in blue were deemed to be unfeasible. c_d^* is the normalized drag coefficient.

Table 3 shows the drag broken down in its main components, the pre-entry drag, ϕ_{pre}, integrated fan cowling viscous force $\phi_{fc,v}$ and pressure force $\phi_{fc,p}$, as well as the MFR and the η_i for the low spillage and high spillage best feasible designs. c_d was normalized by the low spillage design's drag coefficient, whereas ϕ_{pre}, $\phi_{fc,v}$, and $\phi_{fc,p}$ were normalized by the drag force calculated for the low spillage design. It can be noticed that, for the low spillage nacelle, the low ϕ_{pre} is balanced with a backward pressure force, whereas, for the high spillage design, the lip suction effect is expressive, leading to a high forward pressure force, balanced by the higher ϕ_{pre}. The skin friction force is similar for the two types of shapes.

Table 3 – High and low spillage nacelle performance results

Type	c_d^*	ϕ_{pre}^*	$\phi_{fc,v}^*$	$\phi_{fc,p}^*$	MFR	η_i
Low spillage	1.0000	0.6035	0.2331	0.1634	0.804	0.9990
High Spillage	1.0004	2.7980	0.2265	-2.0242	0.634	0.9995

The superscript * refers to normalized values.

Figure 7 shows the Mach number contours for the a) high spillage and b) low spillage designs, whilst Figure 8 depicts the intake and cowl pressure distribution, also for both designs. The pressure coefficient C_P is defined as $(p - p_\infty)/q_\infty$, where p and p_∞ are the local and freestream static pressures, respectively, and q_∞ is the fresstream dynamic pressure. It is shown that, for the high spillage design, there is a high-speed bubble at the front part of the cowling, causing a low-pressure peak and a relatively steep pressure change. Although this does not qualify as a problem at this operating condition, it could lead to supersonic velocities when the nacelle is subjected to incoming flow at an angle of attack. On the other hand, the inlet provides a smoother flow, with lower velocities and lower pressure gradients, when compared to the low spillage case. The low spillage design provides less aggressive pressure gradients at the cowling, but a more intense acceleration inside the inlet, and thus steeper changes in pressure. This is an indication that this inlet would perform poorly at low/speed and high incidence conditions since the pressure gradients at the keel would be significantly intensified.

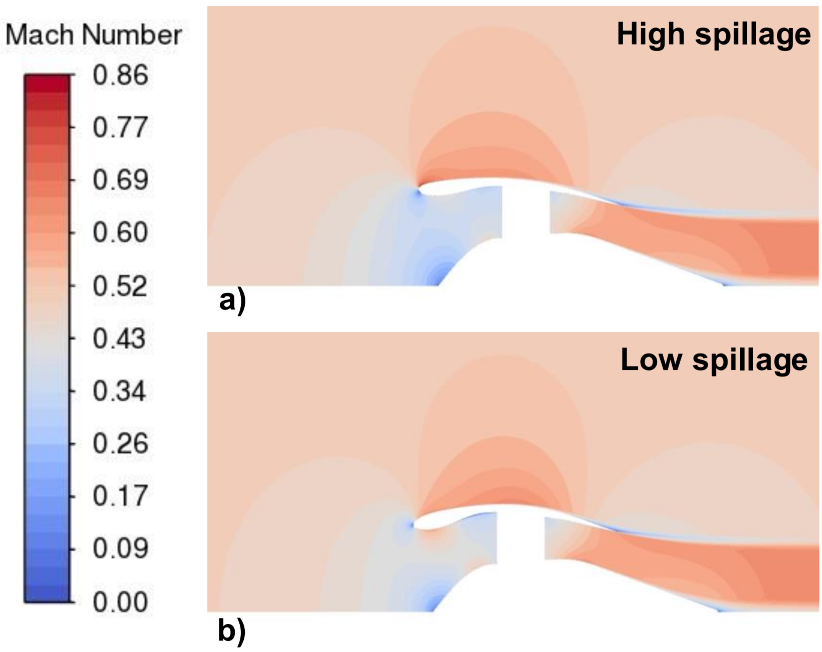

Figure 7 - Mach number contours for a) high spillage and b) low spillage nacelles

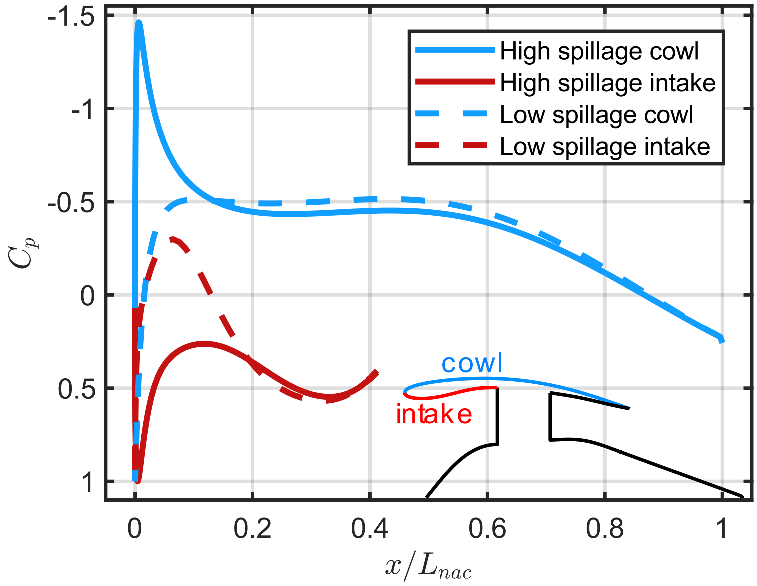

Figure 8 – Intake and cowl pressure distribution for the high spillage and low spillage nacelle designs.

One could anticipate that the aforementioned high-spillage design would perform poorly at cruise, when local incidence is considered, since the cowl acceleration bubble could easily turn into supersonic. However, due to its less cambered shape, and high highlight area, it would be the best choice for takeoff. The low-spillage case, whilst showing better cruise performance, would be problematic for high-incidence conditions, because of its cambered shape that results in a higher misalignment between the incoming flow and the inlet. Such suspicions were confirmed with the 3D studies, which will be discussed in the next section.

3.3 Three dimensional studies

This section brings the major results obtained from the 3D CFD simulations. A short description of the operating conditions is provided in section 2.5.

3.3.1 Cruise

It is well known from turbofan nacelles that drooping the inlet is useful for better alignment of the incoming flow and consequent reduction of drag. Furthermore, drooping can substantially improve the inlet performance at high-incidence conditions [13, 14]. However, most of the drag reduction comes from weakening the shock waves at the cowling and thus it is not clear if drooping can substantially improve the performance of nacelles to be used on electric fans, since, due to the low M_∞, shocks are not likely to be present at cowl. Four test cases were prepared using the low and high spillage geometries obtained from the optimization studies. A droop of 3 degrees ($\theta_d = 3^o$) was applied to the symmetric high spillage geometry, here referred to as HS1, to generate the drooped high spillage geometry HS2. Similarly, the symmetric low spillage geometry is named LS1 and the drooped low spillage one LS2.

Figure 9 shows the Mach number contours for the aforementioned designs operating at cruise, with $AoA = 4^o$. For better visualization, the high spillage and low spillage cases are presented in different color scales. For the same reason, the maximum Mach number of the contour plots is limited to 1.0, although it reaches up to 1.17 in HS1. It can be noticed that supersonic velocities were attained in case HS1, whereas figure 9b shows that drooping the inlet attenuates the phenomena for HS2. This occurs because the incoming streamlines are better aligned with the nacelle camber line at the leading edge, reducing the local incidence. Although the supersonic velocities in HS1 are not severe enough to generate strong shock waves, a slightly increased flight Mach number or angle of attack could be problematic and increase significantly the wave drag. For the low spillage cases LS1 and LS2, shown respectively in figures 9c and 9d, it can be seen that drooping provides a better alignment of the incoming flow with the inlet, contributing mainly to reduce the speed outside of the crown's cowling and near the keel's inlet throat.

The pressure distribution for the high spillage and low spillage nacelles is depicted in figure 10 for the crown and keel positions. It is shown in figure 10a that drooping the nacelle reduces the magnitude of the low-pressure peak at the fan cowling at the crown location. This reduces the pressure gradients, the flow acceleration, and ultimately the drag. The opposite behavior is observed at the keel, in figure 10b, where steeper pressure changes can be observed for the drooped nacelle. Similar, but less intense, behavior can be observed for the low spillage cases, shown in figure 10c and figure 10d, for the crown and keel locations, respectively. For the low spillage case, dropping the nacelle reduced drag by 1.18%, whilst for the high spillage case a drag reduction of 1.45% was observed.

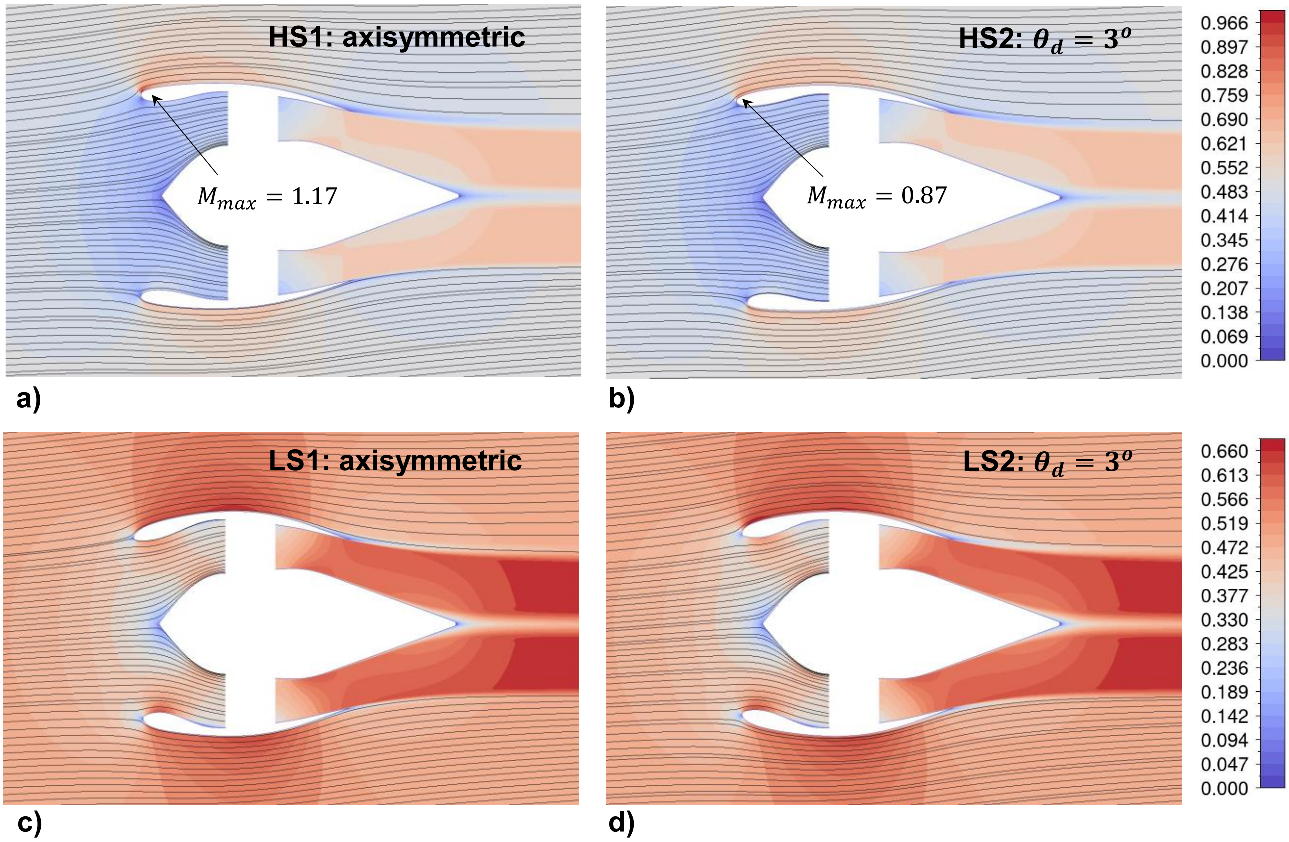

Figure 9 – Mach number contours for a) High spillage symmetric geometry HS1, b) high spillage drooped geometry HS2, c) low spillage symmetric geometry LS1, and d) low speed drooped geometry LS2, for the cruise operating condition with $AoA = 4^o$.

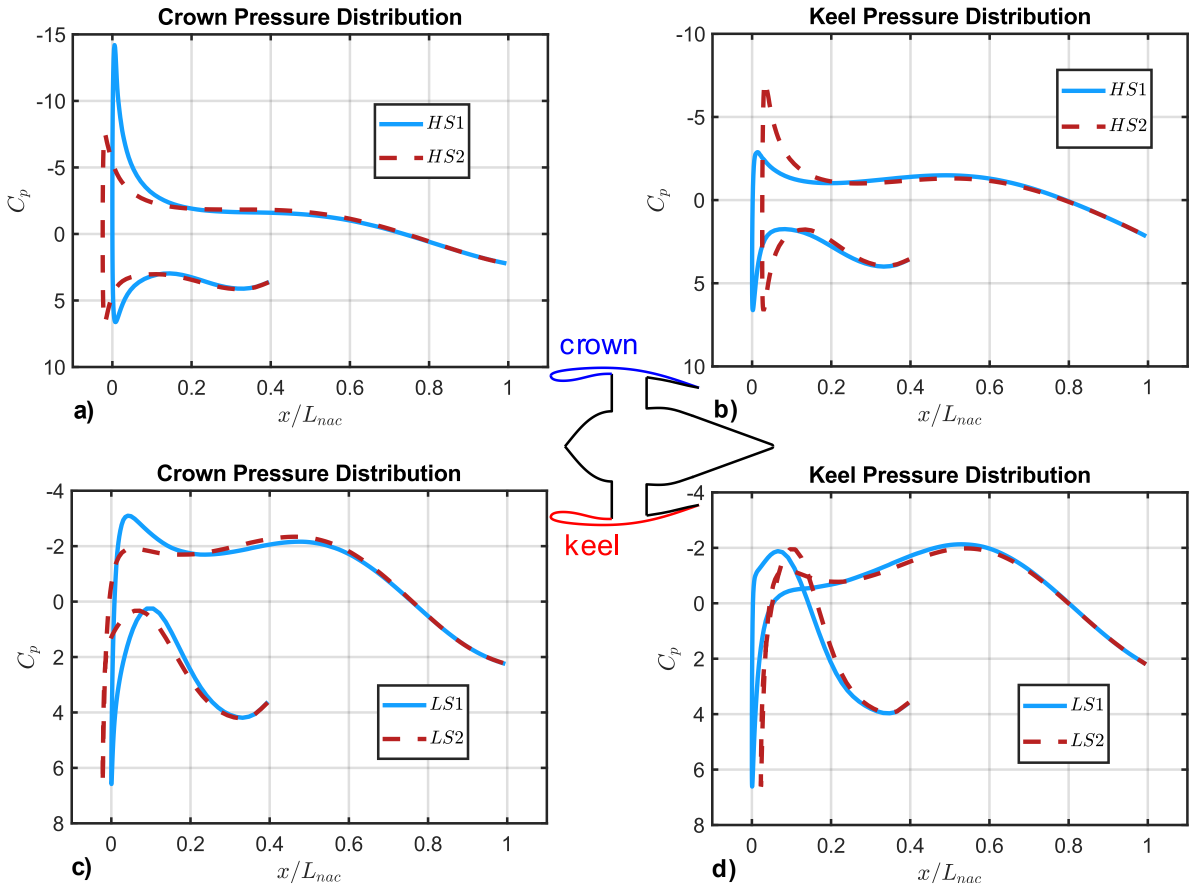

Figure 10 – Pressure distribution for the a) high spillage designs at the crown, b) high spillage designs at the keel, c) low spillage designs at the crown, d) lows spillage designs at the keel, for the cruise operating condition with $AoA = 4^o$.

3.3.2 Takeoff

The high speed and low speed symmetric and drooped cases were tested for an end-of-runway takeoff condition, described in section 2.5. An additional low spillage shape was generated for this study. The nacelle LS2 was modified at the keel position by increasing the r_{hi}/r_{fan} parameter by 7.5%, thus generating the geometry referred to as LS3.

The Mach number contours for the takeoff condition are shown in figure 11. Fully attached flow was attained in cases HS1 and HS2, shown in figures 11a and 11b, respectively. It is shown in figure 11c that, for LS1, a strong separation is occurring, starting from the keel's highlight position. For case LS2, figure 11d, the flow accelerates around the lower lip, and starts to separate near the throat position. It is noticeable that separation was attenuated with the drooping of the low spillage inlet. Finally, the modification in r_{hi}/r_{fan} results in fully attached flow as shown in figure 11e.

Figure 12 indicates that the high spillage designs (figure 12a) have less severe pressure gradients inside the inlet when compared to the low spillage ones (figure 12b), and therefore, for the former, the flow accelerates gradually around the lower lip, whilst keeping itself attached to the inlet surface. Figure 12b, when analyzed along with figure 11, shows that that separation is strongly linked to how steep is the pressure rise inside the inlet. In case LS1, the increase in pressure is so abrupt that the flow does not have enough momentum to turn around the lip and consequently separates next to the highlight location. Drooping the inlet, in case LS2, improves the lip suction, allowing the flow to start turning around the lip, however separation occurs near the throat. Finally, by increasing r_{hi}/r_{fan} at the keel location, the increase in pressure becomes more gradual, the lip suction is increased, and the flow is maintained fully attached. This occurs because the keel profile becomes less cambered at the leading edge, better aligning the inlet with the incoming flow and providing a smoother change in curvature for the streamlines to follow.

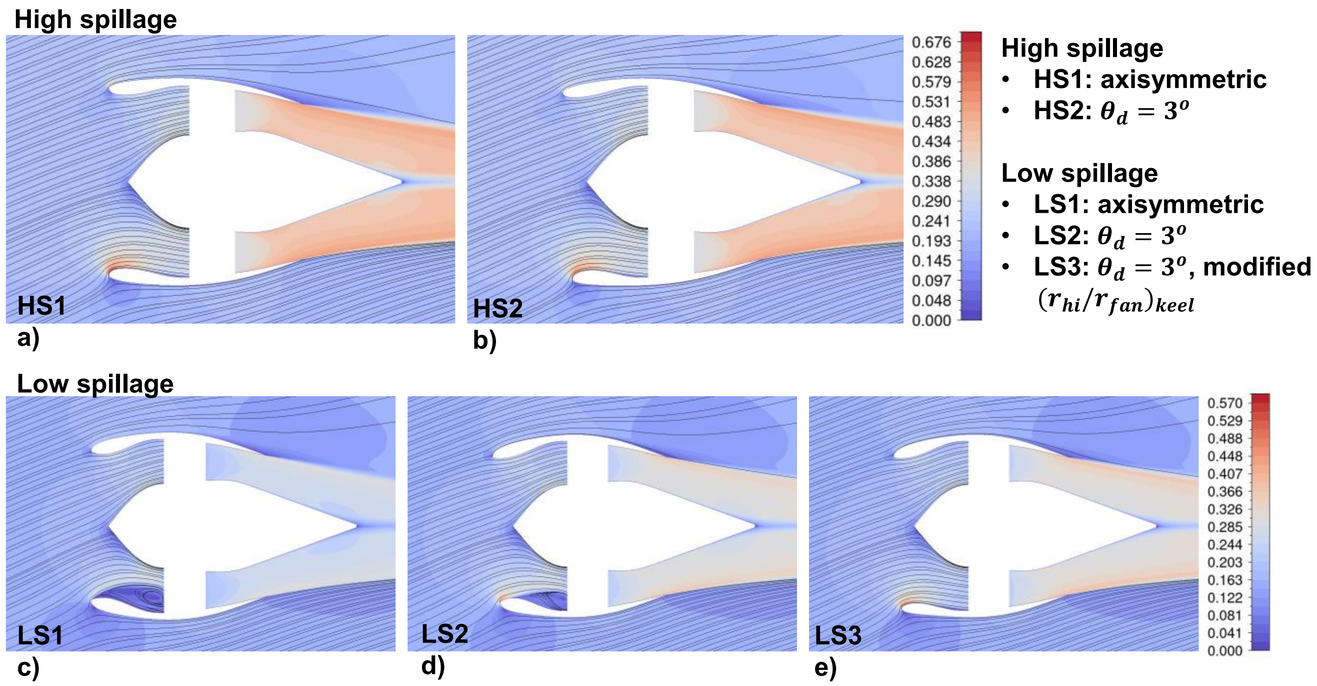

Figure 11 - Mach number contours for a) High spillage symmetric geometry HS1, b) high spillage drooped geometry HS2, c) low spillage symmetric geometry LS1, d) low speed drooped geometry LS2, and d) low speed drooped geometry with modified keel LS3, for the takeoff operating condition with $AoA = 22^o$.

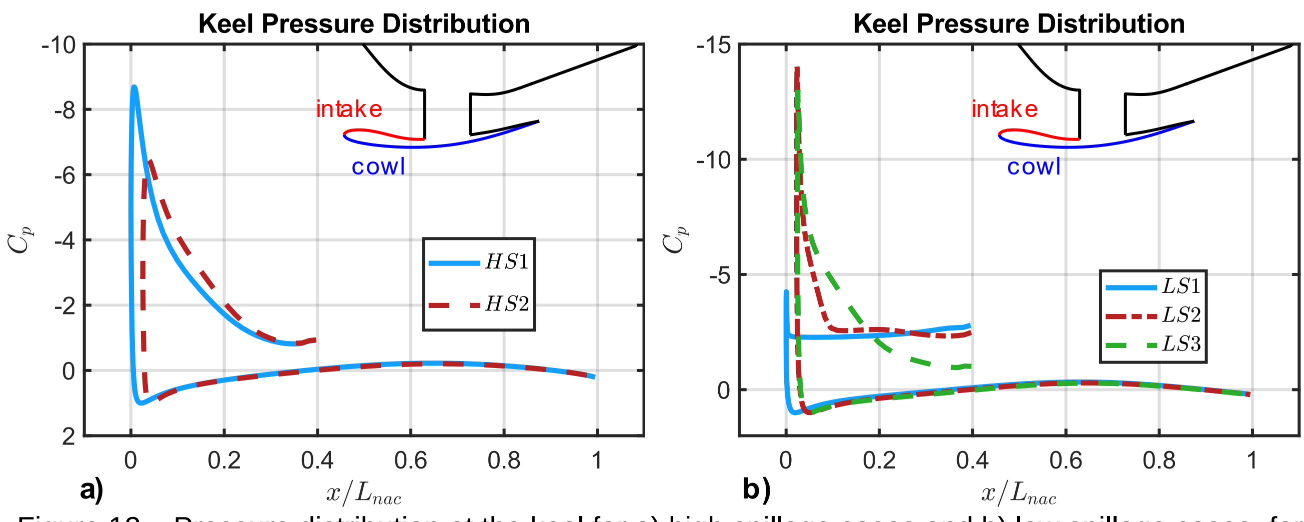

Figure 12 – Pressure distribution at the keel for a) high spillage cases and b) low spillage cases, for the takeoff operating condition with $AoA = 22^o$.

The inlet performance parameters for the aforementioned cases are presented in table 4. As expected, the values of DC_{60} are low for the cases HS1, HS2 and LS3 where the flow is fully attached. For cases LS1 and LS2, where separation is observed, distortion is high. It can be observed that, in case LS2, only drooping the inlet reduced DC_{60} from 0.4632 to 0.2166. The same pattern can be observed for η_i: the stronger the separation and higher the distortion, the lower η_i will be. The MFR at takeoff is expected to be higher than 1, due to the higher mass flows and lower freestream speeds. In case LS1, where distortion is severe, a decrease in mass flow is observed, and consequently the MFR is reduced. A lower MFR is obtained in case LS3 compared to case LS2, and this is a direct consequence of increasing the highlight area for design LS3.

Table 4 – Inlet performance parameters for the takeoff test cases.

Case	DC_{60}	MFR	η_i
HS1	0.0147	1.1104	0.9994
HS2	0.0147	1.1098	0.9995
LS1	0.4632	1.1526	0.9924
LS2	0.2166	1.3488	0.9976
LS3	0.0208	1.3014	0.9992

Designs HS1, HS2 and LS3 would all be good design choices. However, HS2 is the recommended one. Firstly, because it provides lower drag than HS1 at cruise. Secondly, due to its less cambered shape, it ought to perform better in low speed off-design conditions not covered in this paper, such as crosswind. Finally, it is not hard to anticipate that the modification done to LS3's keel will be penalized with a drag increase at cruise. It is worth highlighting that the high spillage and low spillage cases are extreme designs. One could choose a more conservative approach for the optimization, attaining more balanced designs. Fixing the r_{hi}/r_{fan} parameter to obtain a constant MFR throughout the design space would be an option.

4. Conclusions

This paper presented the initial design efforts of designing an efficient and robust nacelle for an electric fan. A multipoint design procedure was employed where two operating conditions were considered: cruise and an end of runway takeoff condition. Initially the nacelle and nozzle shapes were optimized for the cruise condition, with aid of 2D axisymmetric CFD simulations. It was found that two types of shapes, which differed significantly in geometry, were the best designs found by the optimizer. They were referred to as low spillage and high spillage cases. The next step was to proceed with the non-axisymmetric design for cruise, considering local incidence, and for takeoff at high AoA. Fully 3D CFD simulations were necessary for this step. Supersonic velocities were observed for the high spillage cases when subjected to $AoA = 4^o$, this issue was solved by drooping the inlet. On the other hand, the high spillage design performed well at takeoff, with low levels of distortion and no observed separation. Whilst a low spillage design performed well at cruise, at takeoff it presented severe levels of distortion, and required to be drooped and have its keel profile modified to become separation free. In face if its superior performance at takeoff, the drooped high spillage design denoted HS2 in this paper was recommended.

The initial design practice was considered successful; however, more steps are recommended before the decision for a definitive geometry is taken. It would be valuable to include the crosswind operating condition into the design loop, and it would also be required to carry out CFD simulations of the obtained optimal nacelle design together with the actual geometry of the fan blades, since differences between the MPC method and the actual flow field are expected.

5. Acknowledgements

This research work was funded by the Swedish National Aviation Engineering Research Program, NFFP, supported by Swedish Armed Forces, the Swedish Defense Materiel Administration, Swedish Governmental Agency for Innovation Systems (VINNOVA), and GKN Aerospace. All the computations were performed using Chalmers Center for Computational Science and Engineering (C3SE) resources, provided by Swedish National Infrastructure for Computing (SNIC).

6. Copyright Statement

References

[1] Van der Sman, E. S., B. Peerlings, J. Kos, R. Lieshout, and T. Boonekamp. "Destination 2050." (2020).

[2] CFM International. "CFM RISE Program - Revolutionary Innovation for Sustainable Engines." (2021).

[3] Bari, Musab, Christy Roof, Amit Oza, and B. Chudobay. "The future of electric aircraft." In *Proceedings of the 51st AIAA Aerospace Sciences Meeting, Grapevine, TX*, pp. 7-10. 2013.

[4] Wroblewski, Gabrielle E., and Phillip J. Ansell. "Mission analysis and emissions for conventional and hybrid-electric commercial transport aircraft." *Journal of Aircraft* 56, no. 3 (2019): 1200-1213.

[5] Huang, Zhongjie, Huadong Yao, Anders Lundbladh, and Lars Davidson. "Low-Noise Propeller Design for Quiet Electric Aircraft." In *AIAA AVIATION 2020 FORUM*, p. 2596. 2020.

[6] Christie, Robert, Alexander Heidebrecht, and David MacManus. "An automated approach to nacelle parameterization using intuitive class shape transformation curves." *Journal of Engineering for Gas Turbines and Power* 139, no. 6 (2017).

[7] Christie, Robert, Matthew Robinson, Fernando Tejero, and David G. MacManus. "The use of hybrid intuitive class shape transformation curves in aerodynamic design." *Aerospace Science and Technology* 95 (2019): 105473.

[8] Tejero, Fernando, Robert Christie, David MacManus, and Christopher Sheaf. "Non-axisymmetric aero-engine nacelle design by surrogate-based methods." *Aerospace Science and Technology* 117 (2021): 106890.

[9] Tejero, Fernando, Matthew Robinson, David G. MacManus, and Christopher Sheaf. "Multi-objective optimisation of short nacelles for high bypass ratio engines." *Aerospace Science and Technology* 91 (2019): 410-421.

[10] Goulos, Ioannis, Tomasz Stankowski, John Otter, David MacManus, Nicholas Grech, and Christopher Sheaf. "Aerodynamic design of separate-jet exhausts for future civil aero-engines—Part I: Parametric geometry definition and computational fluid dynamics approach." *Journal of Engineering for Gas Turbines and Power* 138, no. 8 (2016).

[11] Goulos, Ioannis, John Otter, Tomasz Stankowski, David MacManus, Nicholas Grech, and Christopher Sheaf. "Aerodynamic design of separate-jet exhausts for future civil aero-engines—Part II: design space exploration, surrogate modeling, and optimization." *Journal of Engineering for Gas Turbines and Power* 138, no. 8 (2016).

[12] Otter, John J., Robert Christie, Ioannis Goulos, David G. MacManus, and Nicholas Grech. "Parametric design of non-axisymmetric separate-jet aero-engine exhaust systems." *Aerospace Science and Technology* 93 (2019): 105186.

[13] Silva, Vinícius T., Anders Lundbladh, Olivier Petit, and Carlos Xisto. "Multipoint Aerodynamic Design of Ultrashort Nacelles for Ultrahigh-Bypass-Ratio Engines." *Journal of Propulsion and Power* (2022): 1-18.

[14] Peters, Andreas, Zoltán S. Spakovszky, Wesley K. Lord, and Becky Rose. "Ultrashort nacelles for low fan pressure ratio propulsors." *Journal of turbomachinery* 137, no. 2 (2015): 021001.

[15] Kulfan, Brenda M. "Universal parametric geometry representation method." *Journal of aircraft* 45, no. 1 (2008): 142-158.

[16] Zhu, Feng, and Ning Qin. "Intuitive class/shape function parameterization for airfoils." *AIAA journal* 52, no. 1 (2014): 17-25.

[17] Linke-Diesinger, Andreas. *Systems of commercial turbofan engines: an introduction to systems functions*. Springer Science & Business Media, 2008.

[18] Li, Linkai, Yang Liu, and Hui Hu. "An experimental study on dynamic ice accretion process over the surfaces of rotating aero-engine spinners." Experimental Thermal and Fluid Science 109 (2019): 109879.

[19] Malouin, Benoit, Martin Gariépy, Jean-Yves Trépanier, and Éric Laurendeau. "Engine pre-entry thrust and standard net thrust evaluation based on the far-field method." *Aerospace Science and Technology* 45 (2015): 50-59.

[20] Destarac, D., and J. Van Der Vooren. "Drag/thrust analysis of jet-propelled transonic transport aircraft; definition of physical drag components." *Aerospace science and technology* 8, no. 6 (2004): 545-556.

[21] Mikkelsen, Kevin L., David J. Myren, Derek G. Dahl, and Monica Christiansen. "Initial subscale performance measurements of the AIAA dual separate flow reference (DSFR) nozzle." In *51st AIAA/SAE/ASEE Joint Propulsion Conference*, p. 3883. 2015.